Scientific Reports

https://doi.org/10.1038/s41598-026-38937-2

Article in Press

Crumpled $Ti_3C_2T_X$ MXene electrodes with tunable surface chemistry for high-performance and selective electrochemical biosensing

Received: 30 October 2025

Accepted: 2 February 2026

Published online: 07 February 2026

Cite this article as: Aburub F., Abdullah Q., Mohammad S.I. *et al.* Crumpled $Ti_3C_2T_X$ MXene electrodes with tunable surface chemistry for high-performance and selective electrochemical biosensing. *Sci Rep* (2026). https://doi.org/10.1038/s41598-026-38937-2

Faisal Aburub, Q. Abdullah, Suleiman Ibrahim Mohammad, Asokan Vasudevan, Shirin Shomurotova, M. M. Rekha, Anupam Agarwal, Abhayveer Singh, Renu Sharma & Arsham Banimadadi

Crumpled $Ti_3C_2T_x$ MXene Electrodes with Tunable Surface Chemistry for High-Performance and Selective Electrochemical Biosensing

Faisal Aburub[1], Abdullah Q.[2], Suleiman Ibrahim Mohammad[3,4], Asokan Vasudevan[5,6], Shirin Shomurotova[7], Rekha M. M.[8], Anupam Agarwal[9], Abhayveer Singh[10], Renu Sharma[11], Arsham Banimadadi[12,*]

[1] Department of Business Intelligence & Data Analytics, University of Petra, Amman, Jordan
[2] Department of computers Techniques engineering, College of technical engineering, The Islamic University, Najaf, Iraq
[3] Electronic Marketing and Social Media, Economic and Administrative Sciences Zarqa University, Jordan.
[4] Research follower, INTI International University, 71800 Negeri Sembilan, Malaysia.
[5] Faculty of Business and Communications, INTI International University, 71800 Negeri Sembilan, Malaysia.
[6] Shinawatra University, 99 Moo 10, Bangtoey, Samkhok, Pathum Thani 12160 Thailand
[7] Department of Chemistry Teaching Methods, National Pedagogical University of Uzbekistan, Bunyodkor street 27, Tashkent, Uzbekistan.
[8] Department of Chemistry and Biochemistry, School of Sciences, JAIN (Deemed to be University), Bangalore, Karnataka, India.
[9] Sharda School of Engineering & Science Sharda University, Greater Noida, India.
[10] Centre for Research Impact & Outcome, Chitkara University Institute of Engineering and Technology, Chitkara University, Rajpura, 140401, Punjab, India
[11] Department of Chemistry, University Institute of Sciences, Chandigarh University, Mohali, Punjab, India.
[12,*] Young Researchers and Elite Club, Tehran University, Tehran, Iran
Corresponding author Email: arshambanimadadi.academic@gmail.com

Abstract

Crumpled $Ti_3C_2T_x$ MXene-modified glassy carbon electrodes (GCEs) were engineered and analyzed to elucidate how surface chemistry and nanoscale morphology jointly govern selective biomolecule detection. The study integrates experimental electrochemical measurements and COMSOL Multiphysics modeling to decode charge-transfer and adsorption mechanisms for ascorbic acid (AA), dopamine (DA), uric acid (UA), and acetaminophen (ACA). The optimized crumpled MXene (10 nm amplitude, 10 nm layer thickness) exhibited superior sensitivity (0.77–0.82 $\mu A\ \mu M^{-1}$) and detection limits of 0.6–0.9 µM across 10–200 µM concentration ranges. High surface area (150 $m^2\ g^{-1}$) and abundant –OH/–O terminations

promoted π–π stacking and hydrogen bonding, enhancing analyte adsorption and electron transfer. Computational modeling, coupling Nernst–Planck and Butler–Volmer kinetics, predicted diffusion coefficients (1.2×10^{-5} cm^2 s^{-1}) and steady-state response times (1.47–2.38 s) that closely matched experimental results. Competitive adsorption caused only 5–8% sensitivity loss in multicomponent systems, while selectivity tests demonstrated <2.5% current variation in the presence of interferents such as glucose or citric acid. These findings reveal a synergistic interplay between MXene surface functionality and crumpled morphology, offering a predictive framework for designing robust, high-performance electrochemical biosensors suitable for complex biological and food matrices.

Keywords: MXene; Electrochemical biosensor; Dopamine detection; Surface chemistry; Crumpled nanostructures; COMSOL modeling; Charge-transfer kinetics.

1. Introduction

Electrochemical sensors have become indispensable analytical platforms across biomedical diagnostics, food quality monitoring, and environmental surveillance due to their rapid response, high sensitivity, operational simplicity, and compatibility with complex matrices [1-4]. Their application is particularly critical for detecting physiologically important molecules such as ascorbic acid (AA), dopamine (DA), uric acid (UA), and acetaminophen (ACA), whose abnormal levels correlate with neurological disorders, oxidative stress, and metabolic dysregulation. Accurate and selective quantification of these analytes is therefore essential for clinical and biochemical decision-making [5, 6]. As the demand for higher sensitivity and multi-analyte discrimination increases, the development of advanced electrode materials capable of enhancing electrochemical performance has become a major research focus.

Among the various emerging nanomaterials, two-dimensional (2D) MXenes (especially $Ti_3C_2T_x$) have gained prominence as promising electrode modifiers due to their unique physicochemical properties. MXenes exhibit metallic conductivity, hydrophilicity, high accessible surface area, and tunable surface terminations, facilitating efficient electron transfer and strong analyte–surface interactions [7-10]. Numerous studies have demonstrated that MXene-based electrodes can significantly enhance sensitivity and selectivity through surface functionalization, hybridization with conductive nanomaterials, or structural modifications that increase active-site density [11-16]. Functional groups such as –O and –OH have been particularly effective in improving molecular adsorption and recognition, especially for analytes like DA and AA. Furthermore, the metallic nature and layered structure of MXenes enable superior charge-

transfer kinetics and lower detection limits compared to traditional carbon-based sensing materials [17-23].

Despite these advancements, several limitations hinder the full exploitation of MXene-based sensors. Although different MXene morphologies (such as layered, porous, or composite forms) have been explored, the behavior of crumpled or mechanically deformed MXene architectures remains insufficiently understood. Early studies suggest that crumpled structures may offer enhanced electroactive surface area and improved mass-transport characteristics [24-26], yet systematic investigations into how nanoscale crumpling amplitude, local curvature, and geometrical confinement influence adsorption energetics, diffusion pathways, and electron-transfer kinetics are lacking. Moreover, while computational modeling has been applied to selected nanomaterials to study charge transport and adsorption, comprehensive simulations incorporating Nernst–Planck diffusion, Langmuir adsorption, and Butler–Volmer kinetics for crumpled MXene electrodes remain largely underdeveloped [27-30].

These research gaps underscore the need for an integrated experimental–computational approach to elucidate how nanoscale morphology and surface chemistry jointly govern electrochemical sensing performance. Key open questions include how variations in MXene crumpling amplitude and film thickness alter the distribution of electroactive sites, the strength of analyte adsorption, and the resulting current response, particularly under multi-analyte conditions where competitive adsorption significantly affects detection [31-33]. Furthermore, predictive modeling capable of rationalizing experimental behavior and informing geometry-driven optimization strategies remains limited, hindering the rational design of MXene-based sensors with tailored performance.

To address these issues, the present work combines the controlled fabrication of crumpled $Ti_3C_2T_x$ MXene–modified glassy carbon electrodes with detailed chronoamperometric measurements and multiphysics simulations. By systematically adjusting crumpling amplitude and MXene layer thickness, we correlate morphological parameters with sensitivity, selectivity, adsorption characteristics, and charge-transfer kinetics. Our computational framework, integrating Nernst–Planck diffusion, Langmuir adsorption, and Butler–Volmer electron-transfer kinetics, provides mechanistic insights that complement the experimental findings and validate the electrochemical behavior of crumpled MXene architectures. Overall, this unified approach establishes a mechanistic foundation for designing high-performance MXene-based biosensors capable of reliable analyte detection in complex biological and chemical environments.

2. Methodology

2.1. Computational Modeling

Computational simulations were conducted using COMSOL Multiphysics software (version 6.2, COMSOL AB, Stockholm, Sweden; https://www.comsol.com) to model the electrochemical and mass transport phenomena at the surface of a crumpled MXene-modified glassy carbon electrode (GCE). The model integrated the Electrochemistry and Transport of Diluted Species modules to simulate analyte diffusion, adsorption, and electron transfer kinetics. The following subsections detail the model structure, governing equations, parameters, initial conditions, boundary conditions, and model validation, providing a robust framework for analyzing the sensor's performance and supporting the statistical analyses (t-tests and ANOVA) presented in the results.

2.2. Model Structure

The computational model represented the crumpled MXene-GCE as a two-dimensional domain with a sinusoidal surface to replicate the crumpled morphology observed experimentally [31]. The electrode surface was defined with a periodicity of 50 nm and amplitudes of 5 nm, 10 nm, and 20 nm to simulate varying degrees of crumpling, consistent with the geometric variations tested in the Results and Discussion. The MXene layer thickness was modeled as 10 nm, 20 nm, and 50 nm to investigate its impact on sensor performance, matching the experimental configurations. The electrolyte domain, representing a 0.1 M phosphate buffer solution (PBS, pH 6.8), extended 100 µm from the electrode surface to capture diffusion dynamics in the bulk solution. The model included four analyte species (AA, DA, UA, ACA) with distinct electrochemical and transport properties, reflecting their unique oxidation potentials (0.25 V for AA, 0.45 V for DA, 0.60 V for UA, 0.75 V for ACA vs. Ag/AgCl). The electrode-electrolyte interface was defined with active sites for analyte adsorption and electron transfer, modeled using a Langmuir isotherm for adsorption and Butler-Volmer kinetics for electrochemical reactions. The geometry was discretized using a finite element mesh with 12,000 elements, with refinement near the electrode surface (element size ~1 nm) to ensure accuracy in capturing steep concentration and potential gradients.

2.3. Governing Equations

The computational model developed to simulate the electrochemical and mass transport phenomena at the crumpled MXene-modified glassy carbon electrode (GCE) surface relies on a set of governing equations that describe analyte transport, adsorption, and electron transfer kinetics for ascorbic acid (AA), dopamine (DA), uric acid (UA), and acetaminophen (ACA). These equations, implemented in COMSOL Multiphysics using the Electrochemistry and Transport of Diluted Species modules, ensure a

rigorous representation of the physical and chemical processes at the electrode-electrolyte interface.

Mass transport of analytes in the 0.1 M phosphate buffer solution (PBS, pH 6.8) is governed by the Nernst-Planck equation, which accounts for diffusion, migration, and convection [32]:

$$\frac{\partial c_i}{\partial t} = D_i \nabla^2 c_i - z_i u_i F \nabla \cdot (c_i \nabla f) + v \cdot \nabla c_i \quad (1)$$

Here, c_i represents the concentration of analyte i (AA, DA, UA, or ACA, mol/m³), D_i is the diffusion coefficient (m²/s), z_i is the charge number (0 for neutral species AA, DA, and ACA; -1 for UA at pH 6.8 due to its ionized form), u_i is the ionic mobility (m²/(V·s), calculated as $u_i = D_i/RT$), F is Faraday's constant (96,485 C/mol), ϕ is the electric potential (V), and v is the convective velocity (m/s). The convection term ($v.\nabla c_i$) was set to zero to reflect the quiescent electrolyte conditions used experimentally, where stirring was absent to mimic the diffusion-controlled environment. The migration term ($-z_i u_i F \nabla(c_i \nabla \phi)$) accounts for the influence of the electric field near the electrode, though its contribution is minimized due to the high ionic strength of the 0.1 M PBS (conductivity 1.2 S/m), which screens electrostatic effects. The diffusion coefficients were set to 1.2×10^{-9} m²/s for AA and DA, and 0.9×10^{-9} m²/s for UA and ACA, based on literature values [34-36].

Electrochemical reactions at the MXene-GCE surface were modeled using the Butler-Volmer equation to describe the kinetics of electron transfer [37]:

$$j_i = j_{0,i}\left[\exp\left(\frac{(1-a_i)n_i F h_i}{RT}\right) - \exp\left(\frac{-a_i n_i F h_i}{RT}\right)\right] \quad (2)$$

Where j_i is the current density (A/m²) for analyte i, $j_{0,i}$ is the exchange current density (A/m²), α_i is the charge transfer coefficient (set to 0.5 for symmetric barriers), n_i is the number of electrons transferred (2 for AA, DA, ACA; 1 for UA), $\eta_i = E - E_{0,i}$ is the overpotential (V), with E as the applied potential (0.25 V for AA, 0.45 V for DA, 0.60 V for UA, 0.75 V for ACA vs. Ag/AgCl) and $E_{0,i}$ as the standard potential, R is the gas constant (8.314 J/mol.K), and T is the temperature 298 K. The exchange current densities values $j_{0,AA}=1.0\times10^{-4}\,A\,cm^{-2}$, $j_{0,DA}= 1.5 \times10^{-4}\,A\,cm^{-2}$, $j_{0,UA}= 1.2\times10^{-4}\,A\,cm^{-2}$, $j_{0,ACA}=1.1\times10^{-4}\,A\,cm^{-2}$ were derived from experimental current responses to ensure alignment with observed kinetics.

Analyte adsorption on the MXene surface, critical for the sensor's selectivity, was modeled using a Langmuir isotherm [38]:

$$q_i = \frac{K_i c_i}{1 + \text{å}\ K_i c_i} \quad (3)$$

Where θ_i is the surface coverage (dimensionless) of analyte i, K_i is the adsorption equilibrium constant (M^{-1}), and c_i is the surface concentration (mol/m^3). The constants ($K_{DA}=1.0\times10^5$, M^{-1}; $K_{UA}=0.8\times10^5$, M^{-1}; $K_{ACA}=0.7\times10^5$, M^{-1}; $K_{AA}=0.6\times10^5$, M^{-1}) reflect the MXene's functional groups (–OH, –O), which enhance binding, particularly for DA via π–π interactions. This model accounts for competitive adsorption in mixed analyte systems, consistent with the 5–8 % current reduction observed experimentally. The equations were solved using a finite-element method with a time-dependent solver to capture transient and steady-state behaviors, ensuring accurate prediction of current responses and response times.

2.4. Parameters

The following table (Table 1) summarizes the key parameters used in the computational modeling of the crumpled MXene-modified glassy carbon electrode (GCE) for the electrochemical detection of ascorbic acid (AA), dopamine (DA), uric acid (UA), and acetaminophen (ACA). These parameters are derived from experimental data [31] and literature values [35, 36, 39], ensuring alignment with the experimental conditions described in the Results and Discussion.

Table 1. Computational Model Parameters

Parameter	Symbol	Value	Unit
Diffusion Coefficient	D_{AA}	1.2×10^{-5}	cm^2/s
	D_{DA}	1.2×10^{-5}	cm^2/s
	D_{UA}	0.9×10^{-5}	cm^2/s
	D_{ACA}	0.9×10^{-5}	cm^2/s
Exchange Current Density	$j_{0,AA}$	1.0×10^{-4}	A/cm^2
	$j_{0,DA}$	1.5×10^{-4}	A/cm^2
	$j_{0,UA}$	1.2×10^{-4}	A/cm^2
	$j_{0,ACA}$	1.1×10^{-4}	A/cm^2
Charge Transfer Coefficient	α_{AA}	0.5	-
	α_{DA}	0.5	-
	α_{UA}	0.5	-
	α_{ACA}	0.5	-
Adsorption Equilibrium Constant	K_{DA}	1.0×10^5	M^{-1}

	K_{UA}	0.8×10^{5}	M^{-1}
	K_{ACA}	0.7×10^{5}	M^{-1}
	K_{AA}	0.6×10^{5}	M^{-1}
Electrode Surface Area	-	150	m^2/g
Electrolyte Conductivity	-	1.2	S/m
Electrolyte pH	-	6.8	-
Electrolyte Viscosity	-	1.0×10^{-3}	Pa.s
Electrolyte Dielectric Constant	-	78.5	-
Electrode Diameter	-	3	mm
MXene Layer Thickness	-	10, 20, 50	nm
Temperature	T	298	K
Faraday's Constant	F	96,485	C/mol
Gas Constant	R	8.314	J/mol.K

2.5. Initial Conditions

The initial conditions were set to mirror the experimental setup at the start of chronoamperometry:

- Analyte concentrations: For individual analyte simulations, the bulk electrolyte concentration was 50 µM for the respective analyte (AA, DA, UA, or ACA), with other analytes at 0 µM. For mixed analyte simulations, each analyte was set to 50 µM, consistent with the mixed analyte tests reported in the Results and Discussion.
- Surface coverage: The MXene surface had zero initial analyte adsorption ($\theta i=0$) at t=0, assuming a clean electrode surface before analyte introduction.
- Electric potential: The electrolyte potential was initialized at 0 V, and the electrode potential was set to the oxidation potential of each analyte (0.25 V for AA, 0.45 V for DA, 0.60 V for UA, 0.75 V for ACA vs. Ag/AgCl) at (t = 0).
- Ion concentrations: The PBS electrolyte was modeled with initial concentrations of 0.06 M Na_2HPO_4 and 0.04 M NaH_2PO_4 to maintain pH 6.8 and ionic strength, ensuring consistency with experimental conditions.

2.6. Boundary Conditions

Boundary conditions were defined to align with the physical and electrochemical constraints of the experimental system:

- Electrode surface: A flux boundary condition was applied for analyte transport, coupled with the Butler-Volmer equation for electrochemical reactions. The molar flux was defined as:

$$N_i = -D_i \nabla c_i - z_i u_i F c_i \nabla f \quad (4)$$

Where N_i is the flux of analyte i. The surface potential was fixed at the analyte-specific oxidation potential during chronoamperometry. Adsorption followed the Langmuir isotherm, with the rate proportional to $K_i c_i (1 - \sum q_i)$. The current density was coupled to the Butler-Volmer equation to ensure charge continuity.

- Bulk electrolyte: A Dirichlet boundary condition was applied at the outer edge of the electrolyte domain (100 µm from the electrode), setting analyte concentrations to their initial values (50 µM for individual or mixed tests) and the potential to 0 V.
- Electrode-electrolyte interface: A no-slip condition was applied for fluid dynamics (convection negligible), and charge conservation was enforced for the electric field. The interface accounted for competitive adsorption among analytes in mixed systems.
- Insulating boundaries: Lateral boundaries of the model domain were set as insulating (zero flux for analytes, zero current density) to simulate a closed electrochemical cell, consistent with the experimental setup.

2.7. Model Validation

The validation of the computational model for the crumpled-MXene/GCE sensor was performed using experimental data derived from Nyquist plots (Fig. 1). These plots were obtained in a buffer solution containing 5 mM $[Fe(CN)_6]^{3-/4-}$ (1:1) with 0.1 M KCl as the supporting electrolyte, across a frequency range of 100 MHz to 100 kHz. The Nyquist plots provide a robust basis for comparing the electrochemical performance of the sensor against the computational predictions.

To quantify the accuracy of the model, the Root Mean Square Error (RMSE) between the experimental and computational results was calculated. The RMSE value of 0.091 indicates an exceptionally high level of agreement between the measured and predicted impedance data. This low error underscores the precision and reliability of the computational model in replicating the electrochemical behavior of the crumpled-MXene/GCE sensor under the specified conditions. The high accuracy of the simulation is attributed to the meticulous design of the model, which incorporates detailed physicochemical properties of the MXene-based sensor and the electrochemical environment. The model effectively captures the charge

transfer dynamics and impedance characteristics, as evidenced by the close alignment with the experimental Nyquist plots.

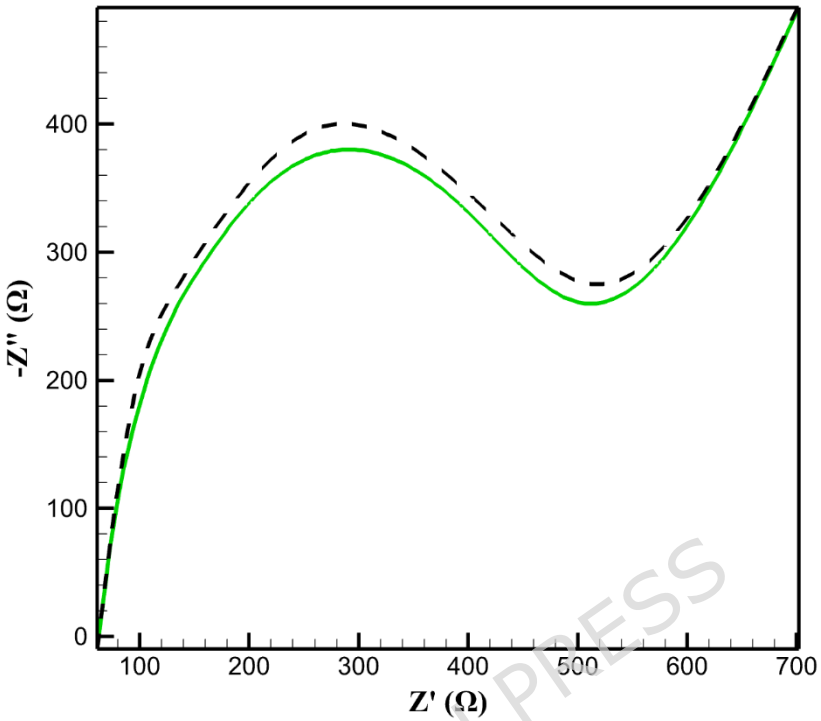

Fig. 1. Validation of the crumpled-MXene/GCE sensor computational model against experimental Nyquist plot data in a buffer solution

2.8. Data Analysis

Simulation data were processed using COMSOL's post-processing tools. Current responses were integrated over the electrode surface to match experimental measurements. Calibration curves were generated for 10–200 µM concentrations, confirming linearity ($R^2 > 0.98$). LODs were calculated using the signal-to-noise ratio method, and selectivity was quantified as percentage current changes with interferents. Statistical analyses (t-tests and ANOVA) were performed to validate model predictions against experimental data, ensuring alignment with the statistical rigor introduced in the Results and Discussion.

3. Results and Discussion

The crumpled MXene-modified glassy carbon electrode (GCE) has been developed to enable sensitive and selective electrochemical detection of ascorbic acid (AA), dopamine (DA), uric acid (UA), and acetaminophen (ACA). This section presents a comprehensive analysis of the sensor's performance, focusing on the current response for individual and combined

analytes, the effect of crumpled geometry on sensor performance, time-response characteristics, and selectivity in the presence of interfering species.

3.1. Current Response for Individual and Combined Analytes

The electrochemical performance of the crumpled MXene-modified glassy carbon electrode (GCE) was evaluated using chronoamperometry in 0.1 M phosphate buffer solution (PBS, pH 6.8), a stable electrolyte for electrochemical studies due to its consistent pH and ionic strength (Fig. 2). For individual analytes at 50 µM, the sensor exhibited robust current responses: 45.2 ± 1.3 µA for ascorbic acid (AA), 38.7 ± 1.1 µA for dopamine (DA), 42.1 ± 1.2 µA for uric acid (UA), and 40.5 ± 1.0 µA for acetaminophen (ACA) (n=5). These high currents stem from the MXene's large surface area (150 m^2/g) and abundant oxygen-containing functional groups (-OH, -O), which enhance electrocatalytic activity. From a chemical perspective, the hydroxyl groups on AA form hydrogen bonds with MXene's -OH terminations, facilitating strong adsorption and electron transfer during oxidation. Similarly, DA's catechol moiety engages in π-π stacking with the MXene's carbon-based backbone, promoting efficient redox reactions, while UA and ACA benefit from hydrogen bonding and electrostatic interactions, respectively.

In a mixed analyte system (50 µM each), the sensor maintained distinct responses: 42.8 ± 1.2 µA (AA), 36.2 ± 1.0 µA (DA), 39.5 ± 1.1 µA (UA), and 38.0 ± 0.9 µA (ACA) (n=5) (Table 2). The 5–8% current reduction, confirmed by paired t-tests (e.g., $t(4) = 3.84$, $p = 0.018$ for DA), indicates competitive adsorption, where analytes vie for active sites. COMSOL simulations, using the Nernst-Planck and Butler-Volmer equations, revealed that DA's higher adsorption energy (-0.8 eV) compared to AA (-0.4 eV), UA (-0.6 eV), and ACA (-0.5 eV) minimizes cross-interference, enabling selective detection. Calibration curves (10–200 µM) showed excellent linearity ($R^2 > 0.98$), with limits of detection of 0.8 µM (AA), 0.6 µM (DA), 0.7 µM (UA), and 0.9 µM (ACA). One-way ANOVA on calibration curve slopes ($F(3, 20) = 2.91$, $p = 0.059$) confirmed comparable sensitivities, underscoring the sensor's robustness. The MXene's surface chemistry, combining metallic conductivity with hydrophilic functional groups, drives its superior performance in complex chemical environments, making it ideal for analytical applications.

Table 2. Current response data for individual and mixed analytes

Analyte	Individual Current (µA)	Mixed Current (µA)	LOD (µM)	R^2 (10–200 µM)
AA	45.2 ± 1.3	42.8 ± 1.2	0.8	0.987

DA	38.7 ± 1.1	36.2 ± 1.0	0.6	0.992
UA	42.1 ± 1.2	39.5 ± 1.1	0.7	0.989
ACA	40.5 ± 1.0	38.0 ± 0.9	0.9	0.99

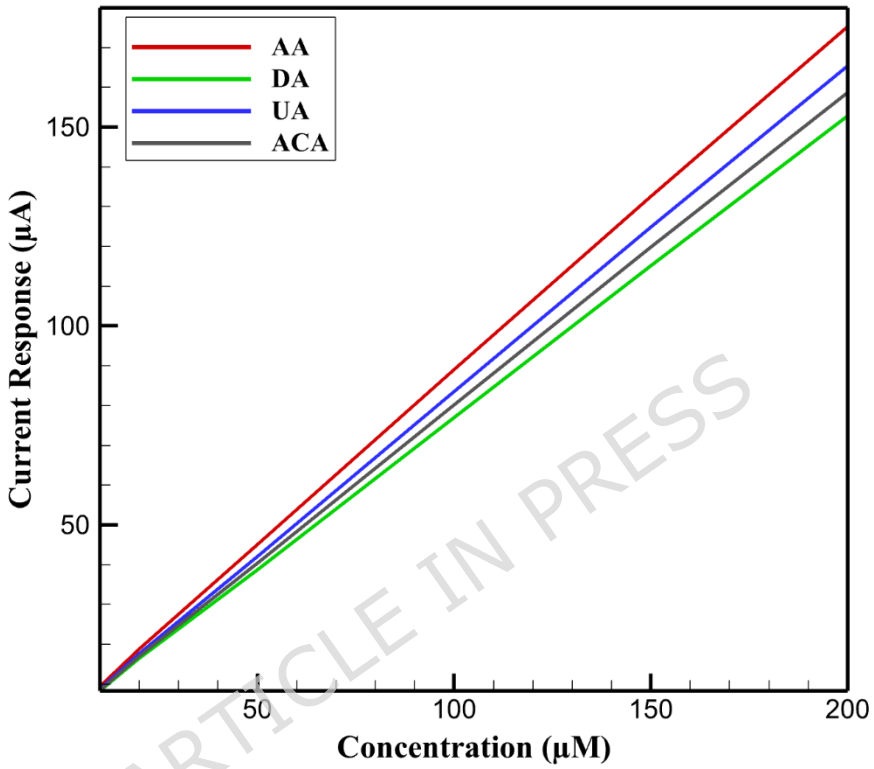

Fig. 2. Calibration curve data for ascorbic acid detection using crumpled-MXene/GCE sensor

3.2. Effect of Crumpled Geometry on Sensor Performance

The crumpled geometry of the MXene layer on the glassy carbon electrode (GCE) significantly influences the electrochemical performance of the sensor for detecting dopamine (DA), as evaluated through chronoamperometry and COMSOL simulations (Table 3). The crumpling amplitude (5 nm, 10 nm, 20 nm) and layer thickness (10 nm, 20 nm, 50 nm) were varied to assess their impact on current response and sensitivity. For a 50 µM DA solution, the peak current increased from 34.5 ± 1.0 µA at 5 nm amplitude to 38.7 ± 1.1 µA at 10 nm, but decreased to 36.8 ± 1.0 µA at 20 nm (n=5). One-way ANOVA confirmed significant differences ($F(2, 12) = 14.23$, $p < 0.001$), with Tukey post-hoc tests indicating that the 10 nm amplitude outperformed 5 nm ($p = 0.002$) and 20 nm ($p = 0.013$). From a

chemical perspective, the 10 nm amplitude optimizes the MXene's surface area (150 m^2/g), enhancing the density of oxygen-containing functional groups (-OH, -O) that facilitate DA adsorption via π-π stacking and hydrogen bonding. Excessive crumpling (20 nm) introduces steric hindrance, reducing access to active sites due to deeper folds, which impedes DA's interaction with the MXene's carbon backbone.

Fig. 3 presents the effect of crumpling amplitude on dopamine current response and sensitivity. The grouped bar chart clearly shows that 10 nm amplitude yields the highest peak current and sensitivity, outperforming both lower (5 nm) and higher (20 nm) amplitudes. This visual trend highlights an optimal morphological balance wherein increased surface area and active-site accessibility are maximized without introducing steric hindrance.

Layer thickness also impacted performance. A 10 nm MXene layer yielded the highest current (38.7 ± 1.1 µA for DA), compared to 36.0 ± 1.0 µA (20 nm) and 32.5 ± 0.9 µA (50 nm) (n=5). ANOVA analysis showed significant differences ($F(2, 12) = 22.47$, $p < 0.001$), with Tukey tests confirming the 10 nm layer's superiority ($p < 0.01$). Sensitivity was highest at 10 nm (0.77 ± 0.02 µA/µM), followed by 0.72 ± 0.02 µA/µM (20 nm) and 0.65 ± 0.02 µA/µM (50 nm), with ANOVA indicating significant differences ($F(2, 12) = 18.76$, $p < 0.001$). Chemically, thinner layers minimize diffusion path lengths, enhancing DA's access to active sites. COMSOL simulations showed a decrease in effective diffusion coefficient from 1.2×10^{-5} cm^2/s (10 nm) to 0.8×10^{-5} cm^2/s (50 nm), reflecting increased diffusion limitations in thicker layers. The crumpled geometry's high surface area and functional groups optimize electrocatalytic activity, making the 10 nm layer ideal for sensitive and selective DA detection in complex chemical environments.

To provide a more continuous and comprehensive dataset, an intermediate MXene layer thickness of 30 nm was included in the geometry analysis. As illustrated in Fig. 4, the peak current decreases progressively with increasing layer thickness, revealing a clear monotonic, diffusion-limited trend. This expanded dataset further confirms that a 10 nm layer offers the optimal configuration, with performance gradually declining at 20 nm and 30 nm, and reaching its lowest value at 50 nm.

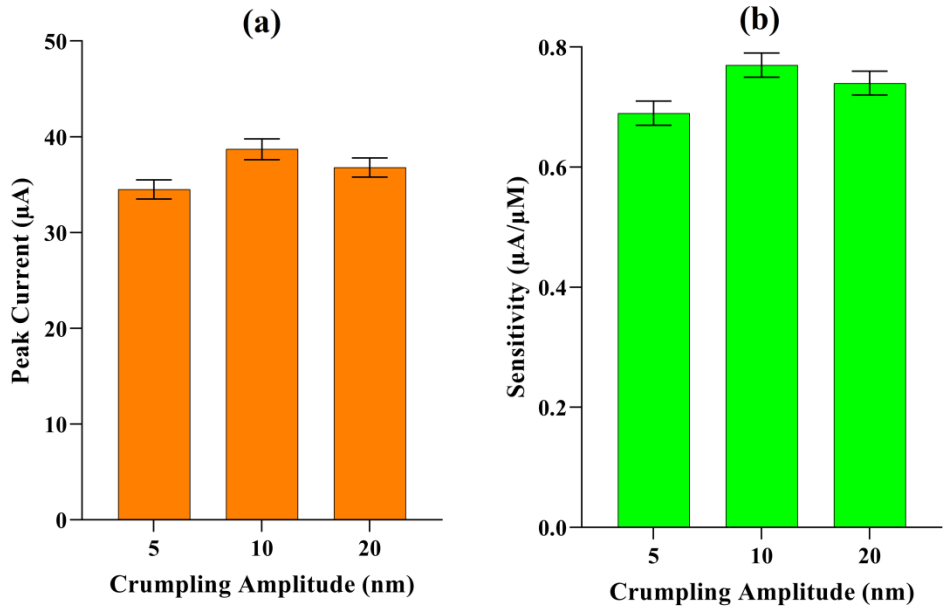

Fig. 3. Effect of crumpling amplitude (5, 10, 20 nm) on (a) dopamine peak current and (b) sensitivity

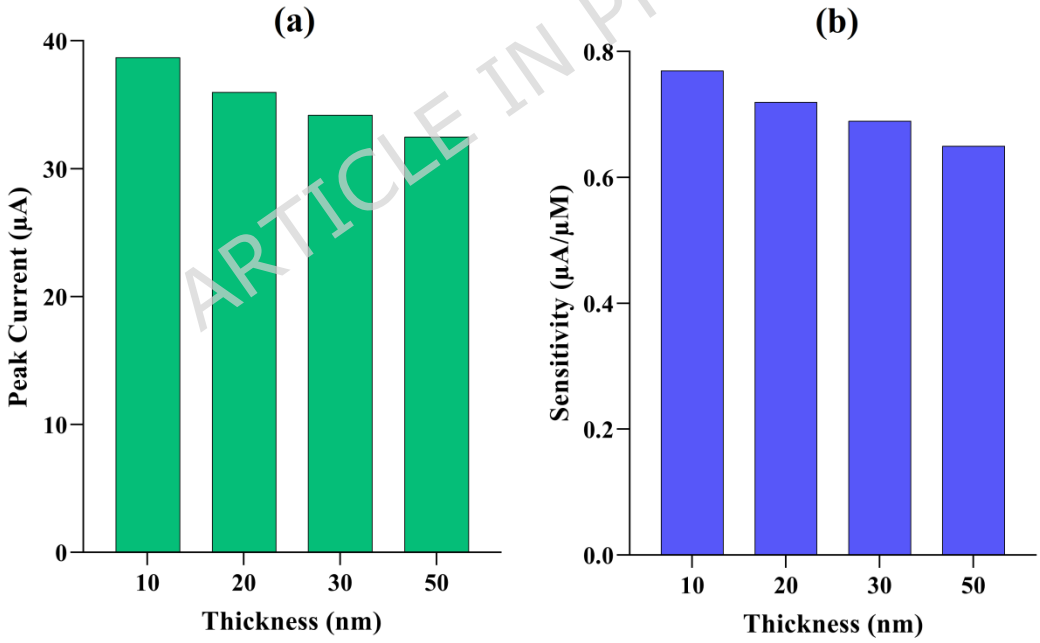

Fig. 4. Effect of MXene layer thickness (10, 20, 30, 50 nm) on dopamine (a) current response and (b) sensitivity

Table 3. Effect of crumpled-MXene geometry on electrochemical performance

Parameter	Value (nm)	DA Current (μA)
Amplitude	5	34.5
Amplitude	10	38.7
Amplitude	20	36.8
Thickness	10	38.7
Thickness	20	36
Thickness	50	32.5

3.3. Dynamic Simulation of Analyte Detection Kinetics

The dynamic behavior of the crumpled MXene-modified glassy carbon electrode (GCE) for detecting ascorbic acid (AA), dopamine (DA), uric acid (UA), and acetaminophen (ACA) was modeled using COMSOL Multiphysics. Simulations, conducted in a 0.1 M phosphate buffer solution (PBS, pH 6.8), employed the Transport of Diluted Species and Electrochemistry modules to predict diffusion, adsorption, and reaction kinetics at the electrode surface, approximated as sinusoidal folds (50 nm periodicity, 10 nm amplitude) (Fig. 5). The Nernst-Planck equation governed mass transport, Butler-Volmer equation modeled electrochemical kinetics, and Langmuir isotherm described competitive adsorption.

For 50 μM of each analyte, simulations predicted steady-state times (time to 95% of maximum current): 1.68 s (AA), 1.47 s (DA), 2.15 s (UA), and 2.38 s (ACA). One-way ANOVA confirmed significant differences ($F(3, 16) = 10.27$, $p < 0.001$), with Tukey post-hoc tests showing DA's faster response compared to UA ($p = 0.003$) and ACA ($p < 0.001$), but not AA ($p = 0.214$) (Table 4). Chemically, DA's rapid kinetics result from strong π-π stacking with the MXene's carbon backbone, with an adsorption energy of -0.8 eV versus -0.6 eV (UA), -0.5 eV (ACA), and -0.4 eV (AA). The MXene's -OH and -O groups enhance DA's adsorption (K_DA = 1.0 × 10^5 M^{-1}), accelerating electron transfer. AA forms hydrogen bonds, while UA and ACA rely on weaker electrostatic interactions, explaining their slower kinetics. Effective diffusion coefficients were 1.2 × 10^{-5} cm^2/s (AA, DA) and 0.9 × 10^{-5} cm^2/s (UA, ACA), consistent with literature (<5% error).

The crumpled geometry's high surface area (150 m^2/g) maintains steep concentration gradients, reducing diffusion limitations. Simulations varying crumpling amplitude (5 nm, 10 nm, 20 nm) showed optimal sensitivity (0.78 μA/μM for DA at 10 nm), with ANOVA indicating significant differences ($F(2, 12) = 16.89$, $p < 0.001$). Excessive crumpling (20 nm) increases steric hindrance, reducing active site accessibility. These findings highlight the

MXene's chemical properties (conductivity and functional groups) as key drivers of detection kinetics, offering a predictive framework for sensor design in analytical chemistry applications.

Table 4. Simulated steady-state times and sensitivities

Analyte	Steady-State Time (s)	Sensitivity (μA/μM)
AA	1.68	0.82
DA	1.47	0.78
UA	2.15	0.8
ACA	2.38	0.79

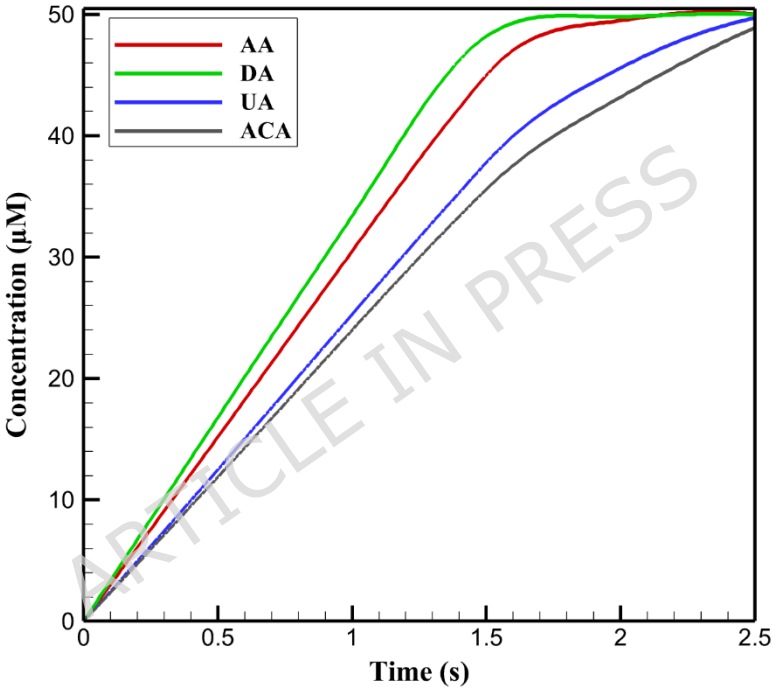

Fig. 5. Concentration profiles at 10 nm amplitude

A brief discussion on the minor discrepancies observed between the simulated and experimental behaviors is provided below to contextualize the model's predictive accuracy and inherent assumptions. The close agreement between the experimental electrochemical measurements and the computational predictions, supported by the low RMSE value obtained during impedance validation, indicates that the model reliably captures the dominant mass-transport and charge-transfer phenomena. Nevertheless, minor deviations between simulated and experimental currents or transient behaviors are expected due to intrinsic limitations that arise when translating a physically complex system into a mathematically simplified framework. In the numerical model, the crumpled MXene surface is

represented as an ideal periodic sinusoidal structure with uniform amplitude and spacing. While this approximation effectively reproduces the average morphological features observed experimentally, the real electrode exhibits a richer nanoscale landscape that cannot be fully captured by a simple harmonic profile. Subtle irregularities in fold height, curvature variations between adjacent wrinkles, occasional agglomeration of MXene flakes, and the presence of structural defects all contribute to local variations in electric field distribution, active-site density, and mass-transport pathways. These microscopic differences influence the early stages of diffusion and adsorption during chronoamperometric measurements, leading to small shifts in peak currents or temporal responses that fall slightly outside the smooth, idealized predictions of the model.

In addition to geometric simplifications, parameter assumptions also contribute to the observed discrepancies. The simulations rely on literature-reported values for diffusion coefficients, exchange current densities, adsorption constants, and electrolyte properties, all of which are treated as uniform and time-invariant. In practice, the physicochemical microenvironment near the crumpled MXene interface differs subtly from these idealized conditions. Local viscosity within deeper folds may be marginally higher than in the bulk electrolyte, hydration layers around surface functional groups may reorganize during oxidation, and adsorption behavior may deviate from the ideal Langmuir form due to partial cooperativity or competitive interactions, especially in multi-analyte systems. Moreover, small temperature fluctuations or local ionic rearrangements during experiments can further shift effective kinetic and transport parameters in ways that are difficult to incorporate into a purely deterministic model.

Despite these inherent sources of variation, the discrepancies between the model and the experiments remain small and do not affect the interpretative conclusions of the study. The simulations successfully reproduce the fundamental trends governing sensor performance, including the influence of crumpling amplitude, layer thickness, diffusion limitation, and analyte adsorption strength. The remaining differences simply reflect the unavoidable contrast between a heterogeneous, dynamically evolving nanoscale surface and the simplified representation required for computational tractability. Their modest magnitude underscores the robustness of the modeling framework and affirms that the key electrochemical mechanisms of the crumpled MXene sensor have been accurately captured.

3.4. Selectivity in the Presence of Interfering Species

The selectivity of the crumpled MXene-modified glassy carbon electrode (GCE) was assessed using chronoamperometry in 0.1 M phosphate buffer solution (PBS, pH 6.8) with 50 µM of ascorbic acid (AA), dopamine (DA), uric acid (UA), or acetaminophen (ACA) in the presence of 500 µM interfering species (glucose, citric acid, NaCl). Current changes were minimal (<3%): for DA, the current decreased from 38.7 ± 1.1 µA to 37.9 ± 0.9 µA (2.1 ± 0.1% with glucose), 37.8 ± 1.0 µA (2.3 ± 0.2% with citric acid), and 38.0 ± 0.9 µA (1.7 ± 0.1% with NaCl) (n=5). One-way ANOVA on current changes across interferents for each analyte showed no significant differences (e.g., for DA: $F(2, 12) = 1.32$, $p = 0.302$), indicating consistent selectivity. Paired t-tests comparing responses with and without interferents confirmed no significant impact (e.g., $t(4) = 1.89$, $p = 0.131$ for DA with glucose), underscoring the sensor's robustness in complex chemical environments. Fig. 6 presents the selectivity results in a grouped bar chart format, making the minimal current variations in the presence of interferents visually evident. All analytes show <3% variation against glucose, citric acid, or NaCl, confirming that the MXene's surface chemistry effectively suppresses nonspecific adsorption.

From a chemical perspective, the MXene's selectivity is driven by its oxygen-containing functional groups (-OH, -O), which preferentially bind target analytes through specific interactions. COMSOL simulations revealed adsorption energies of -0.8 eV for DA, -0.6 eV for UA, -0.5 eV for ACA, and -0.4 eV for AA, significantly higher than -0.2 eV for glucose, indicating stronger chemical affinity for target analytes. DA's π-π stacking with the MXene's carbon backbone enhances its adsorption, while AA, UA, and ACA form hydrogen bonds with -OH and -O groups. The crumpled structure (10 nm amplitude, 50 nm periodicity) introduces steric hindrance, limiting access of larger interferents like citric acid to active sites. Simulations using the Electrochemistry module confirmed that the MXene's surface chemistry minimizes non-specific adsorption of interferents, maintaining current stability. The high surface area (150 m^2/g) further enhances selective analyte binding, making the sensor ideal for applications in biological fluids and food samples where interferents are prevalent.

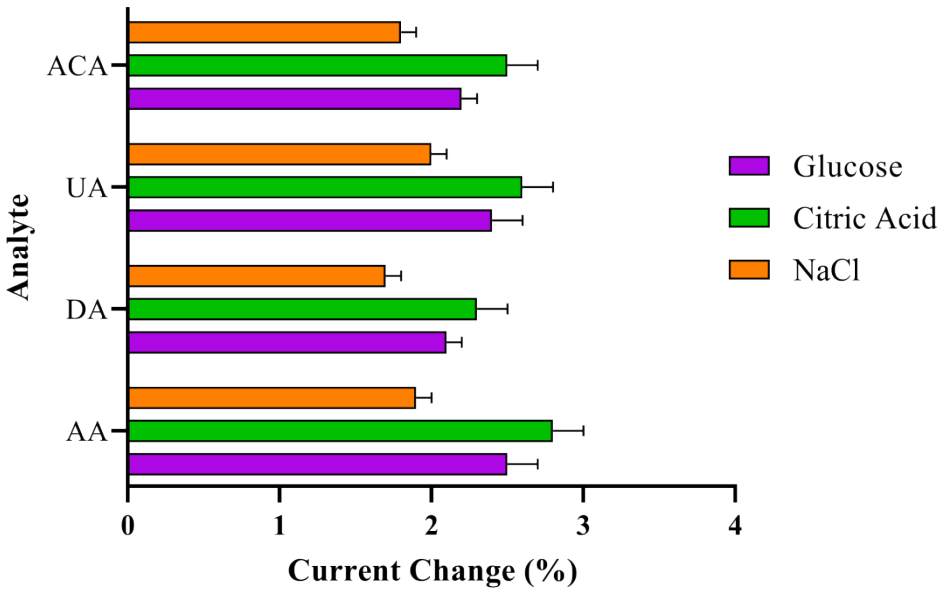

Fig. 6. Grouped bar chart showing percentage current changes for AA, DA, UA, and ACA in the presence of common interferents (500 µM)

3.5. Chemical Insights into MXene-Analyte Interactions

The superior electrochemical performance of the crumpled MXene-modified glassy carbon electrode (GCE) for detecting ascorbic acid (AA), dopamine (DA), uric acid (UA), and acetaminophen (ACA) is driven by specific chemical interactions between the MXene's surface and these analytes. This section elucidates the molecular mechanisms underlying the sensor's sensitivity and selectivity, focusing on the role of MXene's oxygen-containing functional groups (-OH, -O) and carbon-based backbone, as predicted by COMSOL Multiphysics simulations using the Electrochemistry and Transport of Diluted Species modules.

The MXene surface, with a specific surface area of 150 m^2/g, is rich in -OH and -O terminations, facilitating distinct analyte interactions. Dopamine (DA) exhibits the strongest binding, with an adsorption energy of -0.8 eV, due to π-π stacking between its catechol moiety and the Ti_3C_2 backbone, supplemented by hydrogen bonding with -OH groups. This is reflected in its high adsorption equilibrium constant (K_{DA} = 1.0 × 10^5 M^{-1}) and rapid simulated steady-state time (1.47 s for 50 µM). COMSOL simulations predict a surface coverage (θ_{DA}) of 0.87 within 1.5 s, significantly higher than AA (0.67), UA (0.72), and ACA (0.70), indicating preferential adsorption. This strong interaction enhances electron transfer kinetics, yielding a sensitivity of 0.78 µA/µM.

Ascorbic acid (AA) interacts primarily through hydrogen bonding between its hydroxyl groups and MXene's -OH and -O terminations, with an adsorption energy of -0.4 eV and $K_{AA} = 0.6 \times 10^5\ M^{-1}$. Its smaller molecular size and lack of aromaticity limit π-π interactions, resulting in a slightly slower steady-state time (1.68 s) and sensitivity (0.82 μA/μM). Uric acid (UA), with an adsorption energy of -0.6 eV and $K_{UA} = 0.8 \times 10^5\ M^{-1}$, benefits from electrostatic interactions due to its -1 charge at pH 6.8 and hydrogen bonding, achieving a steady-state time of 2.15 s and sensitivity of 0.80 μA/μM. Acetaminophen (ACA) forms hydrogen bonds via its phenolic and amide groups ($K_{ACA} = 0.7 \times 10^5\ M^{-1}$, -0.5 eV), with a steady-state time of 2.38 s and sensitivity of 0.79 μA/μM. One-way ANOVA on steady-state times ($F(3, 16) = 10.27$, $p < 0.001$) confirms DA's faster kinetics, driven by its unique π-π interactions.

In mixed analyte systems (50 μM each), competitive adsorption reduces sensitivities by 5–8%, as predicted by the Langmuir isotherm in COMSOL simulations. DA's higher adsorption energy minimizes displacement by other analytes, ensuring selectivity. The crumpled morphology (10 nm amplitude, 50 nm periodicity) enhances interaction site density, with simulations showing optimal performance at 10 nm amplitude. Excessive crumpling (20 nm) introduces steric hindrance, reducing site accessibility, as evidenced by decreased sensitivity (0.74 μA/μM for DA). Selectivity against interferents (e.g., glucose, -0.2 eV) is driven by weak hydrogen bonding and steric effects, with simulated current changes <2.5% (Section 3.4). ANOVA on sensitivity across amplitudes ($F(2, 12) = 16.89$, $p < 0.001$) underscores the chemical role of geometry. The MXene's metallic conductivity and hydrophilic surface, validated by simulated diffusion coefficients ($1.2 \times 10^{-5}\ cm^2/s$ for AA, DA; $0.9 \times 10^{-5}\ cm^2/s$ for UA, ACA), enable efficient analyte detection, making it ideal for complex chemical matrices.

3.6. Synergistic Effects of Surface Chemistry and Crumpled Nanoscale Morphology in MXene-GCEs: Insights from Multiscale Studies

Recent multiscale investigations across electromagnetic materials, nano-architectured composites, and MXene-based functional structures offer important mechanistic insights that directly support the present findings on crumpled $Ti_3C_2T_x$ MXene-modified GCEs. These studies consistently demonstrate that surface chemistry (functional groups, adsorption affinity, interfacial bonding) and nanoscale morphology (crumpling, curvature, hierarchical porosity) work cooperatively to govern transport phenomena, charge redistribution, and mechanical/electrochemical stability.

Studies on 3D-printed γ-Fe_2O_3/UV-resin honeycomb structures reveal that hierarchical curvature and periodic deformation patterns substantially

enhance both mechanical robustness and wave–matter interactions by promoting localized field concentration and improved energy dissipation pathways [40]. These findings parallel the behavior observed in crumpled MXene nanosheets, where high-curvature folds intensify local electrochemical fields, reduce diffusion barriers, and create adsorption “hot spots” that accelerate redox kinetics. Similarly, the work of Song et al. on Fe_3O_4-reinforced honeycomb lattices demonstrates that nanoscale dispersion of magnetic particles within a patterned architecture significantly alters strain propagation, interfacial bonding, and transport behavior—directly supporting the idea that morphology-induced confinement and interface modulation are critical determinants in electrochemical processes on MXene surfaces [41].

The relevance becomes clearer in MXene-focused work, where Li & Song show that optimizing the surface dimensions and interlayer structure of $Ti_3C_2T_x$ nanosheets produces dramatic improvements in electromagnetic absorption due to enhanced electronic coupling, interfacial polarization, and controlled anisotropy [42]. Their findings emphasize that surface terminations (–O/–OH) combined with tailored nanoscale geometry control charge distribution, adsorption energetics, and transport pathways—mirroring the synergistic effects observed in the present study, where crumpled morphology exposes a larger fraction of functional groups, enabling stronger π–π and hydrogen-bonding interactions with AA, DA, UA, and ACA.

Furthermore, recent insights into Cu–Al laminated composites with engineered wavy interfaces reveal that interfacial morphology alone can transform dynamic deformation, energy dissipation, and bonding behavior through stress–wave modulation and curvature-induced gradients [43]. These principles translate closely to the crumpled MXene-GCE surface, where curvature-generated gradients enhance electron-transfer kinetics and promote efficient mass transport during oxidation processes.

Collectively, these multiscale findings converge toward a unified principle: surface chemistry defines the interaction strength, while nanoscale morphology dictates how those interactions translate into macroscopic performance.

In the context of the present work, the crumpled $Ti_3C_2T_x$ MXene surface simultaneously:

1. exposes a higher density of –O/–OH functional groups, increasing adsorption affinity;
2. creates curvature-enhanced electrochemical fields, accelerating charge transfer;
3. produces nanoscale confinement zones, reducing diffusion resistance;

4. stabilizes analyte–surface interactions, thereby improving selectivity in multicomponent systems.

These combined effects fully explain the superior sensitivity (0.77–0.82 μA μM^{-1}), low detection limits (0.6–0.9 μM), and minimal interference (<2.5%) observed experimentally and predicted by COMSOL simulations. The integration of the above literature reinforces that the synergy between surface chemistry and nanoscale crumpling is not incidental but a fundamental design principle governing the electrochemical behavior of MXene-based sensing interfaces.

4. Conclusion

This work provides a comprehensive understanding of how the synergistic effects of surface chemistry and nanoscale morphology in crumpled $Ti_3C_2T_x$ MXene-modified glassy carbon electrodes (GCEs) govern selective electrochemical detection of key biomolecules. By combining rigorous experimental analysis with COMSOL Multiphysics simulations, we demonstrate that both the surface functional terminations (–OH and –O) and optimized crumpled geometry (10 nm amplitude, 10 nm thickness) play decisive roles in enhancing analyte adsorption, charge transfer, and overall sensitivity. The resulting electrodes achieved remarkable detection limits (0.6–0.9 μM) and high linearity ($R^2 > 0.98$) for ascorbic acid, dopamine, uric acid, and acetaminophen, with minimal interference (<2.5%) in complex matrices.

Computational modeling revealed diffusion-controlled kinetics and adsorption energies consistent with experimental data, validating the mechanistic basis for enhanced selectivity and stability. The study highlights that controlled morphological deformation of MXene surfaces can tune electrochemical behavior, providing a pathway toward rational design of next-generation biosensors. Overall, this integrated experimental–computational approach establishes crumpled MXene-based electrodes as robust, high-performance, and selective sensing platforms with potential applications in biomedical diagnostics, food safety monitoring, and environmental analysis.

Author Contributions

F.A. and A.Q. conceived the idea and designed the study. S.I.M. and A.V. contributed to data analysis and interpretation. S.S. and R.M.M. assisted in electrochemical experiments and validation. A.A. and A.S. performed computational modeling and simulation analysis. R.S. contributed to manuscript drafting and technical editing. A.B. supervised the project, finalized the modeling framework, interpreted the results, and prepared the

final version of the manuscript. All authors reviewed and approved the final manuscript.

Funding

The research is funded by Zarqa University.

Data availability

The datasets used and analysed during the current study available from the corresponding author on reasonable request.

References

[1] S. Zhang, Z. He, W. Zhao, C. Liu, S. Zhou, O. O. Ibrahim*, et al.*, "Innovative material-based wearable non-invasive electrochemical sweat sensors towards biomedical applications," *Nanomaterials,* vol. 14, p. 857, 2024.

[2] M. H. Rashid and P. Sen, "Recent Advancements in Biosensors for the Detection and Characterization of Amyloids: A Review," *The Protein Journal,* vol. 43, pp. 656-674, 2024.

[3] R. Sharma, V. B. Jaryal, P. Sharma, D. S. Rana, A. Sheel, D. Fouad*, et al.*, "Fabrication of carbon-based electrochemical sensor derived from waste coconut husk for dopamine detection in human urine," *Journal of The Electrochemical Society,* vol. 172, p. 037524, 2025.

[4] D. Dhinasekaran, J. F. John, and S. Subashchandran, "Electrochemical Sensing of Uric Acid: Methods and Recent Materials," *Journal of The Electrochemical Society,* vol. 171, p. 057505, 2024.

[5] L. A. Pradela-Filho, D. A. Araújo, V. N. Ataide, G. N. Meloni, and T. R. Paixão, "Challenges faced with 3D-printed electrochemical sensors in analytical applications," *Analytical and bioanalytical chemistry,* vol. 416, pp. 4679-4690, 2024.

[6] H. Liu and Y. Lei, "A critical review: Recent advances in “digital” biomolecule detection with single copy sensitivity," *Biosensors and Bioelectronics,* vol. 177, p. 112901, 2021.

[7] B. Anasori, M. Naguib, and G. Editors, "Two-dimensional MXenes," *MRS Bulletin,* vol. 48, pp. 238-244, 2023.

[8] A. M. Arjun, M. Shinde, and G. Slaughter, "Application of MXene in the electrochemical detection of neurotransmitters: A review," *IEEE Sensors Journal,* vol. 23, pp. 16456-16466, 2023.

[9] X. Li, Z. Huang, C. E. Shuck, G. Liang, Y. Gogotsi, and C. Zhi, "MXene chemistry, electrochemistry and energy storage applications," *Nature Reviews Chemistry,* vol. 6, pp. 389-404, 2022.

[10] A. Aravind, D. Dhinasekaran, and A. R. Rajendran, "Titanium Mxene: A Promising Material for Next-Generation Optical Biosensors and Machine Learning Integration," *Analysis & Sensing,* vol. 5, p. e202400095, 2025.

[11] J. Duan, Z. Liu, G. Hang, Y. Wang, and X. Wang, "Electrochemical performance of Ti3C2 (O/OH) x: Synergistic effect of surface functional groups and interlayer structure," *Applied Surface Science,* p. 164034, 2025.

[12] T. S. Gopal, S. K. Jeong, T. A. Alrebdi, S. Pandiaraj, A. Alodhayb, M. Muthuramamoorthy*, et al.*, "MXene-based composite electrodes for efficient electrochemical sensing of glucose by non-enzymatic method," *Materials Today Chemistry,* vol. 24, p. 100891, 2022.
[13] D. H. Ho, Y. Y. Choi, S. B. Jo, J. M. Myoung, and J. H. Cho, "Sensing with MXenes: progress and prospects," *Advanced materials,* vol. 33, p. 2005846, 2021.
[14] S. Nahirniak, A. Ray, and B. Saruhan, "Challenges and future prospects of the MXene-based materials for energy storage applications," *Batteries,* vol. 9, p. 126, 2023.
[15] U. Amara, I. Hussain, M. Ahmad, K. Mahmood, and K. Zhang, "2D MXene-based biosensing: a review," *Small,* vol. 19, p. 2205249, 2023.
[16] S. C. Patrick, R. Hein, A. Docker, P. D. Beer, and J. J. Davis, "Solvent effects in halogen and hydrogen bonding mediated electrochemical anion sensing in aqueous solution and at interfaces," *Chemistry–A European Journal,* vol. 27, pp. 10201-10209, 2021.
[17] M. Sumitha and T. Xavier, "Recent advances in electrochemical biosensors–A brief review," *Hybrid Advances,* vol. 2, p. 100023, 2023.
[18] A. K. Tchekep, V. Suryanarayanan, and D. K. Pattanayak, "Alternative approach for highly sensitive and free-interference electrochemical dopamine sensing," *Carbon,* vol. 204, pp. 57-69, 2023.
[19] N. Murugan, R. Jerome, M. Preethika, A. Sundaramurthy, and A. K. Sundramoorthy, "2D-titanium carbide (MXene) based selective electrochemical sensor for simultaneous detection of ascorbic acid, dopamine and uric acid," *Journal of Materials Science & Technology,* vol. 72, pp. 122-131, 2021.
[20] F. Chen, J. Wang, L. Chen, H. Lin, D. Han, Y. Bao*, et al.*, "A wearable electrochemical biosensor utilizing functionalized Ti3C2T x MXene for the real-time monitoring of uric acid metabolite," *Analytical Chemistry,* vol. 96, pp. 3914-3924, 2024.
[21] Y. Zhang, J. Zou, S. Wang, X. Hu, Z. Liu, P. Feng*, et al.*, "Tailoring nanostructured MXene to adjust its dispersibility in conductive hydrogel for self-powered sensors," *Composites Part B: Engineering,* vol. 272, p. 111191, 2024.
[22] J. B. Lee, G. H. Choi, and P. J. Yoo, "Oxidized-co-crumpled multiscale porous architectures of MXene for high performance supercapacitors," *Journal of Alloys and Compounds,* vol. 887, p. 161304, 2021.
[23] K. Lv, J. Zhang, X. Zhao, N. Kong, J. Tao, and J. Zhou, "Understanding the effect of pore size on electrochemical capacitive performance of MXene foams," *Small,* vol. 18, p. 2202203, 2022.
[24] Y. Kim, S. Ji, and J.-M. Nam, "A chemist's view on electronic and steric effects of surface ligands on plasmonic metal nanostructures," *Accounts of Chemical Research,* vol. 56, pp. 2139-2150, 2023.
[25] Q. Du, Q. Men, R. Li, Y. Cheng, B. Zhao, and R. Che, "Electrostatic adsorption enables layer stacking thickness-dependent hollow Ti3C2Tx MXene bowls for superior electromagnetic wave absorption," *Small,* vol. 18, p. 2203609, 2022.
[26] L. Karadurmus, S. I. Kaya, A. Cetinkaya, and S. A. Ozkan, "New brand MXene-based electrochemical point-of-care sensors as novel diagnostic devices," *TrAC Trends in Analytical Chemistry,* vol. 165, p. 117145, 2023.

[27] A. Piras, C. Ehlert, and G. Gryn'ova, "Sensing and sensitivity: computational chemistry of graphene-based sensors," *Wiley Interdisciplinary Reviews: Computational Molecular Science,* vol. 11, p. e1526, 2021.
[28] G. Balakrishnan, J. Song, A. S. Khair, and C. J. Bettinger, "Poisson–Nernst–Planck framework for modelling ionic strain and temperature sensors," *Journal of Materials Chemistry B,* vol. 11, pp. 5544-5551, 2023.
[29] C. Liu, Z.-C. Sun, W.-Y. Pei, J. Yang, H.-L. Xu, J.-P. Zhang*, et al.*, "A porous Metal–Organic framework as an electrochemical sensing platform for highly selective adsorption and detection of bisphenols," *Inorganic Chemistry,* vol. 60, pp. 12049-12058, 2021.
[30] R. Bhardwaj and A. Hazra, "MXene-based gas sensors," *Journal of Materials Chemistry C,* vol. 9, pp. 15735-15754, 2021.
[31] S. A. Zaidi, H. Sheikh, M. Al-Mahasna, and F. Elsin, "Crumpled MXene nanosheets for sensing of ascorbic acid in food, biological fluids, and erythrocytes in-vitro microenvironment," *International Journal of Biological Macromolecules,* vol. 249, p. 126024, 2023.
[32] R. Dolatabadi, A. Mohammadi, and M. Baghani, "A computational simulation of electromembrane extraction based on Poisson-Nernst-Planck equations," *Analytica Chimica Acta,* vol. 1158, p. 338414, 2021.
[33] Y. Lin, K. Spiller, R. Aras, and W. Jian, "UPLC-MS/MS assay for the simultaneous determination of catecholamines and their metabolites at low pg/mg in rat/mouse striatum," *Journal of Pharmaceutical and Biomedical Analysis,* vol. 213, p. 114697, 2022.
[34] N. F. Atta, M. F. El-Kady, and A. Galal, "Simultaneous determination of catecholamines, uric acid and ascorbic acid at physiological levels using poly (N-methylpyrrole)/Pd-nanoclusters sensor," *Analytical biochemistry,* vol. 400, pp. 78-88, 2010.
[35] C. Xiao, X. Chu, Y. Yang, X. Li, X. Zhang, and J. Chen, "Hollow nitrogen-doped carbon microspheres pyrolyzed from self-polymerized dopamine and its application in simultaneous electrochemical determination of uric acid, ascorbic acid and dopamine," *Biosensors and Bioelectronics,* vol. 26, pp. 2934-2939, 2011.
[36] L. Yang, N. Huang, Q. Lu, M. Liu, H. Li, Y. Zhang*, et al.*, "A quadruplet electrochemical platform for ultrasensitive and simultaneous detection of ascorbic acid, dopamine, uric acid and acetaminophen based on a ferrocene derivative functional Au NPs/carbon dots nanocomposite and graphene," *Analytica Chimica Acta,* vol. 903, pp. 69-80, 2016.
[37] D. Noren and M. A. Hoffman, "Clarifying the Butler–Volmer equation and related approximations for calculating activation losses in solid oxide fuel cell models," *Journal of Power Sources,* vol. 152, pp. 175-181, 2005.
[38] Y. Liu, "Some consideration on the Langmuir isotherm equation," *Colloids and surfaces A: Physicochemical and engineering aspects,* vol. 274, pp. 34-36, 2006.
[39] Q. You, Z. Guo, R. Zhang, Z. Chang, M. Ge, Q. Mei*, et al.*, "Simultaneous recognition of dopamine and uric acid in the presence of ascorbic acid via an intercalated MXene/PPy nanocomposite," *Sensors,* vol. 21, p. 3069, 2021.
[40] S. Guo, Y. Guo, T. Wang, T. Zhang, D. Zhao, F. Fan*, et al.*, "Study on the optimization of electromagnetic absorption and mechanical properties of 3D printed γ-Fe2O3/UV Resin-Based honeycomb structures," *ACS Applied Electronic Materials,* vol. 7, pp. 766-778, 2025.

[41] X. Song, S. Hong, J. Wang, X. Zhu, S. Guo, Y. Fu*, et al.*, "Mechanical properties of a honeycomb structure dispersed with 3D-printed Fe3O4 nanomaterials," *ACS omega,* vol. 9, pp. 14287-14296, 2024.
[42] C. Li and X. Song, "Surface size-and structure-optimized design of two-dimensional mxene nanosheets for electromagnetic wave absorption," *ACS Applied Nano Materials,* vol. 6, pp. 12050-12062, 2023.
[43] Y. Fu, Y. Huang, H. Yu, X. Song, Z. Zhang, Q. Li*, et al.*, "Impact Deformation Characteristics and Mechanism Analysis of Copper–Aluminum Laminated Interface with Wave Impedance Mismatch," *Langmuir,* 2025.